Theoretical Study of Gold Nanoparticles Randomly Dispersed on a Dielectric/Gold Substrate

Ophélie Saison-Francioso, Gaëtan Lévêque, Abdellatif Akjouj, Yan Pennec

ACS OMEGA

http://pubs.acs.org/journal/acsodf

Article

Theoretical Study of Gold Nanoparticles Randomly Dispersed on a Dielectric/Gold Substrate

Ophélie Saison-Francioso,* Gaëtan Lévêque, Abdellatif Akjouj, and Yan Pennec

Cite This: https://doi.org/10.1021/acsomega.3c00342

Read Online

ACCESS | Metrics & More | Article Recommendations | Supporting Information

ABSTRACT: We theoretically study random arrangements of cylindrical gold nanoparticles (NPs) deposited on a dielectric/gold substrate. We use two methods, namely the Finite Element Method (FEM) and the Coupled Dipole Approximation (CDA) method. The FEM is increasingly used to analyze the optical properties of NPs, but calculations for arrangements containing a large number of NPs have a high computational cost. On the contrary, the CDA has the advantage to drastically reduce the computation time and the memory demand compared to the FEM. Nevertheless, as the CDA involves modeling each NP as a single electric dipole through the polarizability tensor of a spheroidal-shaped NP, it may be an insufficiently accurate method. Therefore, the main purpose of this article is to verify the validity of using the CDA in order to analyze such a kind of nanosystems. Finally, we capitalize on this methodology to draw some tendencies between statistics of NPs' distributions and the plasmonic properties.

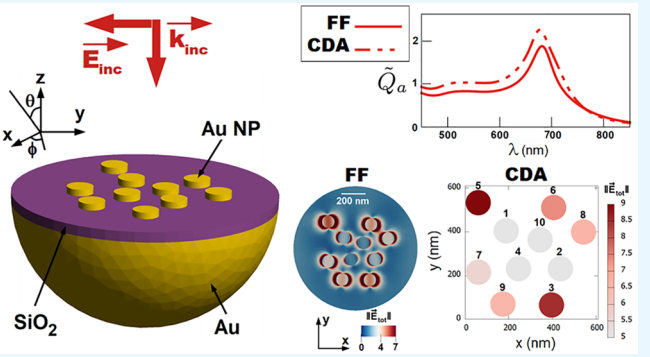

INTRODUCTION

The interaction of light with noble metal nanoparticles (NPs) has been an important experimental and theoretical field of research for a long time.[1−3] Potential applications concern various areas like optical sensing,[4] biomedicine,[5] electronics,[6] and data storage.[7] For NPs, the size of which is smaller than the wavelength of light, the incident electric field can drive the well-known Localized Surface Plasmon Resonances (LSPRs). The excited free electrons of the metal conduction band collectively oscillate and generate an intense electromagnetic field at the NP surface. The incident light is both absorbed and scattered. For a single NP, the spectral response is highly dependent on the size, the shape, the metal composing the NP, and the surrounding environment.[8−11] For a set of NPs, the individual plasmonic response is also influenced by the interparticle electromagnetic coupling. There are two kinds of interactions: the near-field and the far-field coupling.[12] The near-field coupling results from the interaction between the evanescent fields confined at the NPs surface and therefore only occurs for small interparticle distances. The far-field coupling comes from the fields scattered by the NPs which are of dipolar character for NPs much smaller than the incident light wavelength.

In this work, we theoretically study random arrangements of cylindrical gold NPs deposited on a dielectric/gold substrate. Nanocylinders or nanodisks are commonly studied structures in the field of plasmonics, both experimentally and theoretically.[13−15] In recent years, disordered arrangements of NPs have drawn attention.[16,17] Just like the surrounding medium, the NPs size, shape, and composition, the arrangement pattern allows the manipulation of the LSPRs optical characteristics. Different disordered structures have already been proposed targeting properties like light trapping.[18] The underlying physics is very rich and the question of the definition and the quantification of the disorder is a vast subject of exploration. The numerical modeling of random configurations is not an easy task due to symmetry breaking. Simulations are quickly computationally expensive and time-consuming, making the study of systems with hundreds of NPs complicated. To overcome this difficulty, it would be interesting to develop methods to quickly understand and elucidate the main features of the arrangements leading to metasurfaces with promising properties. This is what we propose to do here by assessing if the performance of the Coupled Dipole Approximation method (CDA) is sufficiently reliable. The CDA involves modeling each NP as a single electric dipole through the polarizability tensor of a spheroidal-shaped NP. As a consequence, the method may be insufficiently accurate. So, to validate this approach, we have carefully compared the results given by the CDA to those

Received: January 17, 2023
Accepted: March 28, 2023

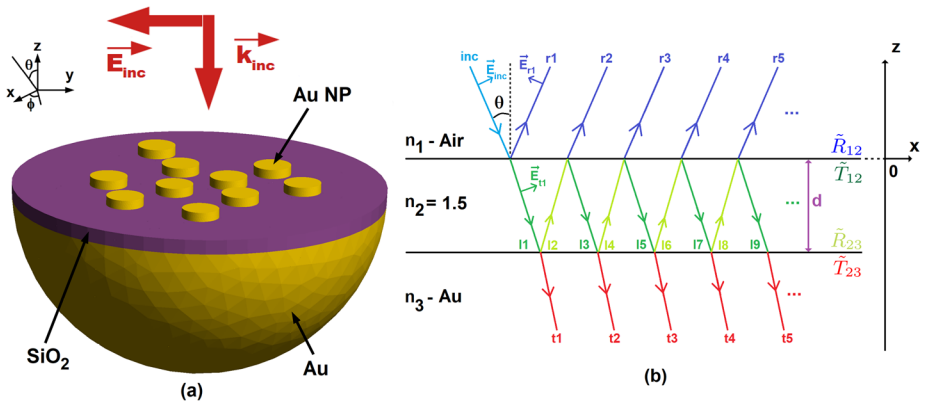

Figure 1. Schematic representation of the system studied (a) and of the background field in the multilayer structure (b).

obtained by the Finite Element Method. The CDA has the advantage to drastically reduce the computation time and the memory demand. The program we have developed allows us to obtain the plasmonic response of a system made up of 50 NPs in 11 h. Moreover, the code being sequential, its performance can be improved by using parallel programming frameworks that can be applied in multicore CPUs[19] or GPUs.[20] This would make it possible to study systems made up of a large number of NPs.

METHOD

System Studied. We study random arrangements of cylindrical gold NPs (Figure 1a). The number of NPs is denoted by the letter N. All the NPs have the same radius r = 50 nm and the same height h = 25 nm. The NPs are deposited on a bilayer substrate made up of a dielectric layer, for which the thickness is d = 40 nm and refractive index is n_2 = 1.5, and a semi-infinite gold layer. The transverse magnetic incident light propagates along the (Oz) axis (θ = 0) and the electric field is polarized along the (Ox) axis. The gold relative dielectric permittivity is described by a Lorentz−Drude model:[21]

$$\varepsilon_{gold}(\omega) = \varepsilon_r(\infty) + \omega_p^2 \sum_{m=0}^{2} \frac{f_m}{\omega_{0,m}^2 - \omega^2 - j\omega\Gamma_m} \tag{1}$$

where $\varepsilon_r(\infty)$ is the dielectric constant at infinite frequency, ω_p is the bulk plasma pulsation, f_m is the strength of the m^{th} Lorentzian damped harmonic oscillator, $\omega_{0,m}$ corresponds to interband transition pulsations (m = 1, 2), and Γ_m are damping pulsations. The parameter values used for the calculations are those of reference 21 and are given in the Supporting Information (SI).

Finite Element Method. FEM has been adequately described elsewhere.[22,23] Our calculations are realized with the help of the high level multiphysics finite element software FreeFEM, developed at the Laboratoire Jacques-Louis Lions of Pierre and Marie Curie University (Paris).[24] To create geometries and unstructured tetrahedral meshes of the systems studied, we use Gmsh which is an open-source 3-D finite element grid generator.[25] The mesh size is adjusted to have a minimum of 4 grid layers along the height of the NPs and below the NPs in the dielectric layer which ensures the numerical accuracy. More details about the convergence are in the Supporting Information. We developed our own FreeFEM script in order to solve the vector wave equation for the time-harmonic scattered electric field.[26] The total field in the presence of the NPs is expressed as the sum of the incident field and the scattered field.[27,28] The weak formulation of the problem is the following:

$$\iiint_{\Omega} [(\vec{\nabla} \wedge \overrightarrow{E_{sca}}).(\vec{\nabla} \wedge \vec{v})\Lambda^{-1} - \varepsilon(\vec{r})k_0^2 \Lambda \overrightarrow{E_{sca}}.\vec{v}]\, d\Omega = \sum_{i=1}^{N} \iiint_{\Omega_{NP_i}} (\varepsilon_{gold} - \varepsilon_{air})k_0^2 \overrightarrow{E_b}.\vec{v}\, d\Omega_{NP_i} \tag{2}$$

where k_0 is the free-space wavenumber, $\varepsilon(\vec{r})$ is the relative permittivity which depends on the position and $\vec{v}$ is a test function which belongs to the finite dimensional vector space where the approximate solution is searched. In our simulations, we use second-order Nédélec tetrahedral finite elements[29] as they fit the physical continuity properties of the electric field across interelement interfaces (continuous tangential components and discontinuous normal components). We seek for $\overrightarrow{E_{sca}}$, the scattered field. The symbol Ω_{NP_i} represents the volume occupied by the NP identified by the letter i. The symbol Ω represents the whole domain which is surrounded by spherical perfectly matched layers (PMLs).[23] The coefficient Λ is equal to 1 outside the PMLs and is a complex number inside the PMLs in order to avoid reflections at the edge of the computational domain. The background field $\overrightarrow{E_b}$ is known everywhere in the planar multilayer structure (Figure 1b):

*In the air layer:

$$\overrightarrow{E_{b1}} = \frac{E_0\, e^{j(k_x x + k_y y)}}{k_1} \begin{pmatrix} k_{1z}\cos(\Phi)(e^{-jk_{1z}z} - \tilde{R}_{12}\, e^{+jk_{1z}z}) \\ k_{1z}\sin(\Phi)(e^{-jk_{1z}z} - \tilde{R}_{12}\, e^{+jk_{1z}z}) \\ k_s(e^{-jk_{1z}z} + \tilde{R}_{12}\, e^{+jk_{1z}z}) \end{pmatrix},$$

$$\tilde{R}_{12} = \frac{r_{12} + r_{23}\, e^{j2k_{2z}d}}{1 + r_{12}r_{23}\, e^{j2k_{2z}d}} \tag{3}$$

*In the dielectric layer:

$$\overrightarrow{E_{b2}} = \frac{E_0\, e^{j(k_x x + k_y y)}}{k_2} \begin{pmatrix} k_{2z}\cos(\Phi)(\tilde{T}_{12}\, e^{-jk_{2z}z} - \tilde{R}_{23}\, e^{+jk_{2z}z}) \\ k_{2z}\sin(\Phi)(\tilde{T}_{12}\, e^{-jk_{2z}z} - \tilde{R}_{23}\, e^{+jk_{2z}z}) \\ k_s(\tilde{T}_{12}\, e^{-jk_{2z}z} + \tilde{R}_{23}\, e^{+jk_{2z}z}) \end{pmatrix},$$

$$\tilde{T}_{12} = \frac{t_{12}}{1 + r_{12}r_{23}\, e^{j2k_{2z}d}},\ \tilde{R}_{23} = \frac{t_{12}r_{23}\, e^{jk_{2z}d}}{1 + r_{12}r_{23}\, e^{j2k_{2z}d}} \tag{4}$$

https://doi.org/10.1021/acsomega.3c00342
ACS Omega XXXX, XXX, XXX−XXX

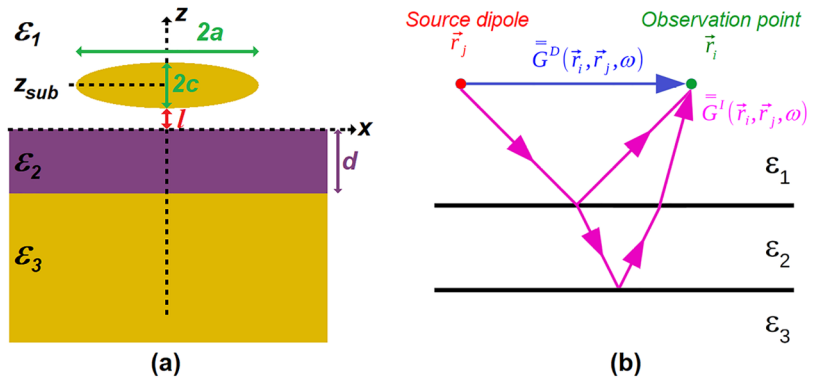

Figure 2. (a) Cross-section of the geometry used in the CDA. (b) Schematic representation of the two contributions of the Green tensors for the planar multilayer system.

*In the gold layer:

$$\overrightarrow{E_{b3}} = \frac{E_0\, e^{j(k_x x + k_y y)}}{k_3} \begin{pmatrix} k_{3z}\cos(\Phi)\tilde{T}_{23}\, e^{-jk_{3z}z} \\ k_{3z}\sin(\Phi)\tilde{T}_{23}\, e^{-jk_{3z}z} \\ k_s \tilde{T}_{23}\, e^{-jk_{3z}z} \end{pmatrix},$$

$$\tilde{T}_{23} = \frac{t_{12}t_{23}\, e^{jk_{2z}d}}{1 + r_{12}r_{23}\, e^{j2k_{2z}d}} \quad (5)$$

where E_0 is the amplitude of the incident electric field, $k_i = n_i k_0$ with $i = 1, 2, 3$, $k_x = k_1 \sin(\theta)\cos(\Phi)$, $k_y = k_1 \sin(\theta)\sin(\Phi)$, $k_s = \sqrt{k_x^2 + k_y^2}$, r_{12}, r_{23}, t_{12}, t_{23} are the Fresnel coefficients for the TM fields.[30] The z component of the wave vector is

$$k_{iz} = \begin{cases} \sqrt{k_i^2 - k_s^2} & \text{if } k_s < k_i \\ j\sqrt{k_s^2 - k_i^2} & \text{if } k_s > k_i \end{cases}, \quad i = 1, 2 \quad (6)$$

$$k_{3z} = A + j\frac{Im(\varepsilon_{gold})k_0^2}{2A},$$

$$A = \sqrt{\frac{B + \sqrt{B^2 + (Im(\varepsilon_{gold})k_0^2)^2}}{2}},$$

$$B = Re(\varepsilon_{gold})k_0^2 - k_s^2 \quad (7)$$

Coupled Dipole Approximation. The nanocylinders are replaced by oblate spheroids for which the semiaxes are $a = b$ and c (Figure 2a). The optical response of the NPs is described by their polarizality tensor $\bar{\bar{\alpha}}$. It is diagonal in the basis $(\hat{x}, \hat{y}, \hat{z})$:

$$\alpha_{ii} = \frac{4}{3}\pi abc \frac{\varepsilon_{gold} - \varepsilon_1}{\varepsilon_1 + L_i'(\varepsilon_{gold} - \varepsilon_1)}, \quad i = x, y, z \quad (8)$$

where L_i' are axis-dependent geometrical factors associated with the NP depolarization. Their expression includes electrodynamic corrections as the size of the NPs studied is too large to strictly satisfy the quasi-static approximation:[31]

$$L_i' = L_i - \frac{D_i V}{4\pi d_i}k_1^2 - j\frac{V}{6\pi}k_1^3, \quad i = x, y, z \quad (9)$$

where V is the spheroid volume, L_i is the well-known static geometrical factors,[32] d_i factors correspond to the length of the semiaxis of the spheroids ($d_x = d_y = a$, $d_z = c$) and D_i is the dynamic geometrical factors. The expression of these factors is given in the SI. The correction in k_1^2 is a dynamic depolarization term which redshifts the plasmonic resonance and comes from the phase difference between the radiations emitted by the different parts of the NP. The correction in k_1^3 is a radiative correction term which corresponds to an attenuation correction specific to any oscillating dipole due to radiation losses. It induces a broadening of the plasmonic resonance.

The dipolar model leads to an overestimation of the electrostatic interaction between the NPs, described as point-dipoles, and their image-dipoles in the substrate.[11] Indeed, if the NPs lie directly on the top of the substrate, this results in a larger redshift of the plasmon resonance than expected, particularly for flat NPs. The overestimation of the effect of the substrate on the NPs can be reduced by artificially moving the NPs away from the substrate. That is why in this study, the NPs are "floating" at a distance l from the substrate (Figure 2a). The coupling between the NPs is modeled using Green's tensors which link the source dipoles to the electric fields they generate at any point $\vec{r}$ in space:

$$\overrightarrow{E_i} = \mu_0\omega^2(\bar{\bar{G}}^D(\vec{r}_i, \vec{r}_j, \omega) + \bar{\bar{G}}^I(\vec{r}_i, \vec{r}_j, \omega))\cdot\vec{p}_j \quad (10)$$

where $\vec{E}_i$ is the electric field radiated in $\vec{r}_i$ by the dipole j situated in $\vec{r}_j$ and μ_0 is the vacuum permeability. Green's tensors contain all the information relating to the unperturbed multilayer system, i.e., in the absence of the NPs, in which the radiations propagate. They are composed by two contributions[33] (Figure 2b):

(1) a direct contribution $\bar{\bar{G}}^D$ which corresponds to the Green's tensor for an infinite homogeneous medium of permittivity ε_1, i.e., the layer where the NPs are situated. This contribution represents the direct coupling between the NPs in the air and can be calculated analytically.[34]

$$\bar{\bar{G}}^D(\vec{r}_i, \vec{r}_j, \omega) = \left(\bar{\bar{I}} + \frac{jk_1R - 1}{k_1^2R^2}\bar{\bar{I}} + \frac{3 - 3jk_1R - k_1^2R^2}{k_1^2R^4}\vec{R}\otimes\vec{R}\right)\frac{e^{jk_1R}}{4\pi R} \quad (11)$$

where $\bar{\bar{I}}$ is the identity matrix of size 3 and $R = \|\vec{r}_i - \vec{r}_j\|$ is the distance between the dipole i and the dipole j.

(2) an indirect contribution $\bar{\bar{G}}^I$ which corresponds to the contribution of the reflected, refracted, and transmitted fields by all the interfaces of the multilayer system.[30,35] It represents the indirect coupling between the NPs through the substrate and must be evaluated numerically.

https://doi.org/10.1021/acsomega.3c00342
ACS Omega XXXX, XXX, XXX−XXX

$$\bar{\bar{G}}^{I}(\vec{r}_i, \vec{r}_j, \omega) = \frac{j}{8\pi^2}\int_{-\infty}^{+\infty}\int_{-\infty}^{+\infty}\frac{1}{k_{1z}}(\tilde{R}_{12}^{TE}\hat{\mathbf{l}}(+k_{1z}) \otimes \hat{\mathbf{l}}(-k_{1z}) + \tilde{R}_{12}^{TM}\hat{\mathbf{m}}(+k_{1z}) \otimes \hat{\mathbf{m}}(-k_{1z}))\, e^{j\vec{k}_s\cdot(\vec{r}_{s,i}-\vec{r}_{s,j})}\, e^{jk_{1z}(z_i+z_j)}\, dk_x\, dk_y \quad (12)$$

where $\tilde{R}_{12}^{TM}$ and $\tilde{R}_{12}^{TE}$ are the reflection coefficients for the multilayer system at the interface air/substrate (eq 3, eq 4). The indirect Green tensor is then obtained in the direct space using the inverse Fourier transform. The unit vectors $\hat{\mathbf{k}}$, $\hat{\mathbf{l}}$, and $\hat{\mathbf{m}}$ form an orthonormal system.[34] They depend on the sign of the z component of the wavevector in order to describe the upward reflection of the downward incident wave.[36] The vector $\hat{\mathbf{l}}$ is perpendicular to the plane defined by $\hat{\mathbf{k}}$ and $\hat{\mathbf{m}}$ and corresponds to TE polarized electric fields, while $\hat{\mathbf{m}}$ corresponds to TM polarized electric fields:

$$\hat{\mathbf{k}}(\pm k_{1z}) = \frac{\vec{k}_1(\pm k_{1z})}{k_1},$$

$$\hat{\mathbf{l}}(\pm k_{1z}) = \frac{\hat{\mathbf{k}}(\pm k_{1z}) \wedge \hat{\mathbf{z}}}{\|\hat{\mathbf{k}}(\pm k_{1z}) \wedge \hat{\mathbf{z}}\|},$$

$$\hat{\mathbf{m}}(\pm k_{1z}) = \hat{\mathbf{k}}(\pm k_{1z}) \wedge \hat{\mathbf{l}}(\pm k_{1z}) \quad (13)$$

The components of the indirect Green tensor as well as details on their calculation are given in the SI. The coupling between the NPs is described by a system of $3N$ linear equations:

$$P = \varepsilon_0\varepsilon_1 A^{-1}E_{inc} \quad (14)$$

where P is a column matrix $(3N \times 1)$ containing the dipole moments of the NPs that we want to calculate. E_{inc} is also a column matrix $(3N \times 1)$ and contains the incident field on each NP which is known. A is the $3N \times 3N$ coupling matrix. The diagonal elements of A correspond to the inverse of the polarizability tensor of the NPs modified by the substrate (see eq 15). As the source point and the observation point coincide, the Green tensor only depends on the position of the NPs along the z axis which is $z_{sub} = l + c$ (Figure 2a). The nondiagonal elements of A represent the interaction between the radiations emitted by the different NPs directly in the air or after reflection on the multilayer substrate ($\bar{\bar{G}} = \bar{\bar{G}}^{D} + \bar{\bar{G}}^{I}$, Figure 2b).

$$A = \begin{pmatrix} \bar{\alpha}^{-1} - k_1^2\bar{\bar{G}}(z_{sub}, \omega) & -k_1^2\bar{\bar{G}}(\vec{r}_1, \vec{r}_2, \omega) & -k_1^2\bar{\bar{G}}(\vec{r}_1, \vec{r}_3, \omega) & \dots & -k_1^2\bar{\bar{G}}(\vec{r}_1, \vec{r}_N, \omega) \\ -k_1^2\bar{\bar{G}}(\vec{r}_2, \vec{r}_1, \omega) & \bar{\alpha}^{-1} - k_1^2\bar{\bar{G}}(z_{sub}, \omega) & -k_1^2\bar{\bar{G}}(\vec{r}_2, \vec{r}_3, \omega) & \dots & -k_1^2\bar{\bar{G}}(\vec{r}_2, \vec{r}_N, \omega) \\ \cdot & \cdot & \cdot & \dots & \cdot \\ \cdot & \cdot & \cdot & \dots & \cdot \\ \cdot & \cdot & \cdot & \dots & \cdot \\ -k_1^2\bar{\bar{G}}(\vec{r}_N, \vec{r}_1, \omega) & -k_1^2\bar{\bar{G}}(\vec{r}_N, \vec{r}_2, \omega) & -k_1^2\bar{\bar{G}}(\vec{r}_N, \vec{r}_3, \omega) & \dots & \bar{\alpha}^{-1} - k_1^2\bar{\bar{G}}(z_{sub}, \omega) \end{pmatrix} \quad (15)$$

RESULTS AND DISCUSSION

Monomer and Dimer. The goal here is to verify if the CDA can be used to study the optical properties of random arrangements of cylindrical gold NPs deposited on a dielectric/gold substrate. The first step is to analyze the case of the monomer (Figure 3). As a reminder, the geometrical parameters of the cylinders are r = 50 nm and h = 25 nm. It is these parameters which are used for the calculations carried out with FreeFEM. For the calculations realized with the CDA, the geometrical parameters of the spheroids are a = 57.2 nm and c = 14.3 nm. They were determined with respect to the following equalities:

$$\begin{cases} V_{sph} = V_{cyl} \\ R_{sph} = \dfrac{c}{a} = R_{cyl} = \dfrac{h}{2r} \end{cases} \quad (16)$$

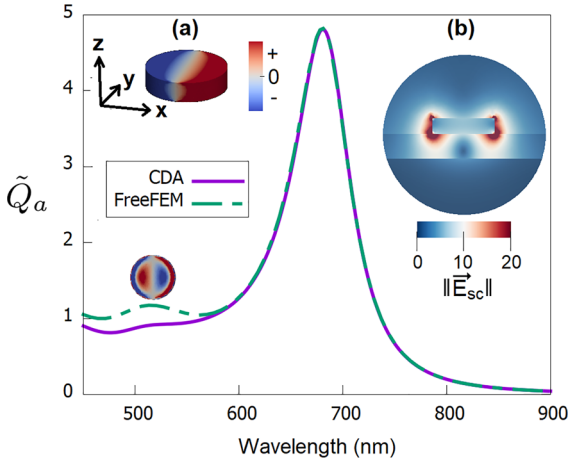

Figure 3. Comparison of the dimensionless absorption efficiency $\tilde{Q}_a$ computed with the CDA (solid line) and with FreeFEM (dashed line) for the monomer. The surface charge distribution (real part) (a) and the scattered field map (b) obtained with FreeFEM at λ_{res} = 681 nm are represented in the insets. To allow visualization, the color scales have been truncated.

where V_{sph}, V_{cyl}, R_{sph}, and R_{cyl} are, respectively, the volume of the spheroids, the volume of the cylinders, the aspect ratio of the spheroids, and the aspect ratio of the cylinders. The distance between the spheroids and the substrate is adjusted to best fit the position of the resonance obtained with FreeFEM and is fixed at l = 13 nm. We see in Figure 3 the absorption spectra of the monomer provided by FreeFEM and the CDA. The absorbed power Q_a is calculated using the following formula:[37]

$$Q_a = -\frac{\omega}{2}\sum_{i=1}^{N} Im(\vec{p}_i^{\,*}\cdot\bar{\bar{\alpha}}_{STAT}^{-1}\cdot\vec{p}_i)(W) \quad (17)$$

, where $\bar{\bar{\alpha}}_{STAT}$ is the static spheroid polarizability. In order to obtain the dimensionless absorption efficiency $\tilde{Q}_a$, the absorbed power is then divided by the incident energy flux $(\varepsilon_0 E_0^2 c)$ and the geometrical cross section of all the NPs:

https://doi.org/10.1021/acsomega.3c00342
ACS Omega XXXX, XXX, XXX−XXX

$$\tilde{Q}_a = \frac{Q_a}{\varepsilon_0 E_0^2 c \times NS} \quad S = \pi a^2 \text{ or } \pi r^2 \text{ for } \theta = 0 \tag{18}$$

In this work, the peak that interests us is the dominant peak which corresponds to the dipolar plasmonic mode as seen on the charge distribution map (Figure 3, inset a). We observe that there is a very good agreement between the two calculation methods concerning the height, the width, and the position of the absorption peak for the dipolar mode. The little peak, mainly visible on the spectra provided by FreeFEM, corresponds to a combination of a dipolar and a breathing mode[38,39] which can be excited through the presence of the metallic layer. Its surface charge distribution at the top face of the NP, shown in Figure 3, is characterized by an admixture of a radial and an azimuthal mode.[40]

Figure 4 describes how the resonance wavelength of the dimer dipolar mode evolves when the center-to-center distance

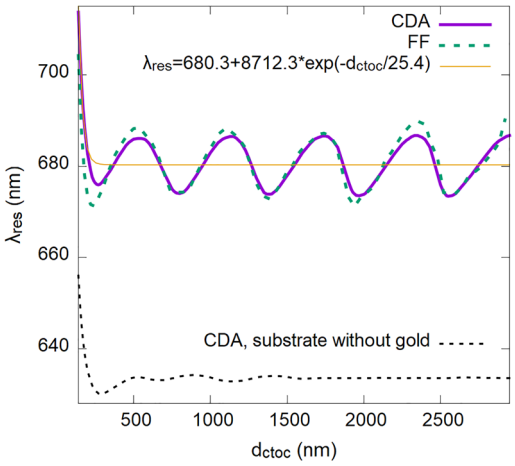

Figure 4. Evolution of the position of the dipolar plasmonic mode of the dimer according to the center-to-center distance.

d_{ctoc} varies. The purple solid line curve was obtained by the CDA method. The green dotted line curve was obtained with FEM. We see that the agreement between the results obtained with the CDA and with FreeFEM is good. However, we notice a curve of less regular appearance for FreeFEM with values moving away from those obtained with the CDA in particular near the extrema. There is also a slight difference between the resonance wavelengths provided by FreeFEM and the CDA at the beginning of the curves. For example, for d_{ctoc} = 140 nm, FreeFEM gives λ_{res} = 704 nm whereas the CDA gives λ_{res} = 714 nm. Indeed, d_{ctoc} is the same for the CDA and FreeFEM calculations. But the semiaxis a of the spheroidal NPs is lightly superior to the radius r of the cylindrical NPs (a = 57.2 nm and r = 50 nm). As a consequence, the edge-to-edge distance is smaller in the CDA case, and the resonance wavelength given by the CDA is higher than that of FreeFEM for the distances allowing near-field coupling. This choice was made in order to obtain a better agreement between the two methods for the monomer and over a wide range of distances for the dimer. We observe two coupling mechanisms when d_{ctoc} varies: the near-field and the far-field coupling.[12] For small interparticle distances, the resonance wavelength exponentially decreases when d_{ctoc} increases. Indeed, the direct dipolar interaction through evanescent fields located on the surface of the NPs (Figure 5a) has a $1/d_{ctoc}^3$ dependence on the NPs separation d_{ctoc}.[41] The near-field coupling can be interpreted by a simple qualitative interpretation. The incident electric field, polarized parallel to the interparticle axis, creates charges of opposite signs on the NP edges facing each other. The attractive forces between the charges oppose the oscillatory motion of the electron cloud, decreasing the oscillation frequency and therefore increasing the resonance wavelength.[42] For larger interparticle distances, the resonance wavelength oscillates. The amplitude of the oscillations is about ten nanometers and increases slightly when d_{ctoc} increases. Relative to the monomer resonance wavelength ($\lambda_{res,\ N=1}$ = 681 nm), we note a less important redshift than the blueshift. The oscillation period can be roughly estimated at 585−605 nm. The radiative coupling comes from the interaction between the scattered fields by the NPs. As a consequence, a standing wave is formed between the NPs (Figure 5b). If antinodes are in front of the evanescent fields at the NPs surface, the dimer resonance wavelength is red-shifted as can be seen on Figure 5b for d_{ctoc} = 900 nm and d_{ctoc} = 1500 nm. If nodes are in front of the evanescent fields at the NPs surface, the dimer resonance wavelength is blueshifted as can be seen on Figure 5b for d_{ctoc}

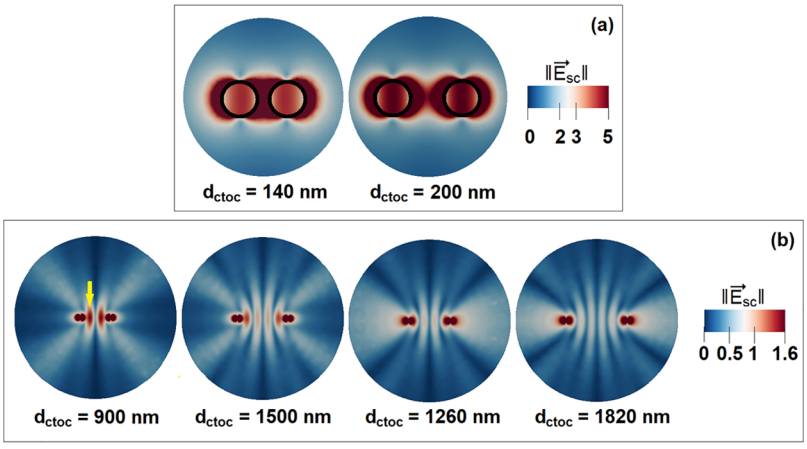

Figure 5. Scattered field maps, obtained with FreeFEM, for different interparticle distances at the dipolar mode resonance wavelength. To allow visualization, the color scales have been truncated. (a) Coupling between the NPs via their evanescent fields. The outline of the NPs is represented by a thick black line. (b) Coupling between the NPs via their radiative fields. The yellow arrow designates an antinode of the standing wave formed between the NPs by the scattered fields.

https://doi.org/10.1021/acsomega.3c00342
ACS Omega XXXX, XXX, XXX−XXX

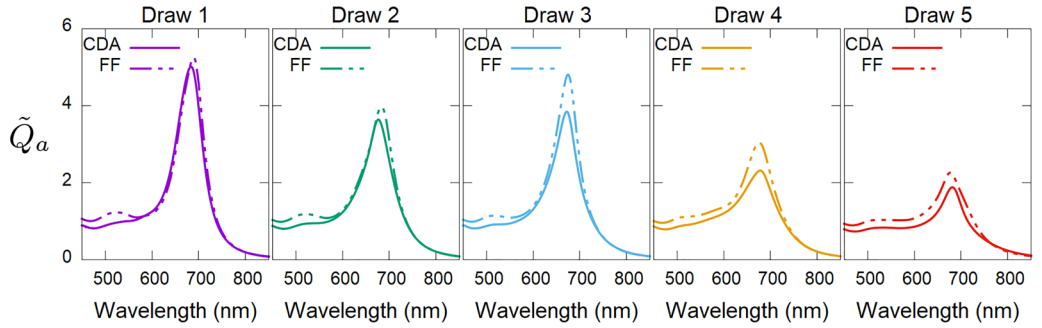

Figure 6. Comparison of the dimensionless absorption efficiency computed with the CDA (solid line) and with FreeFEM (dashed line) for different arrangements of N = 10 NPs.

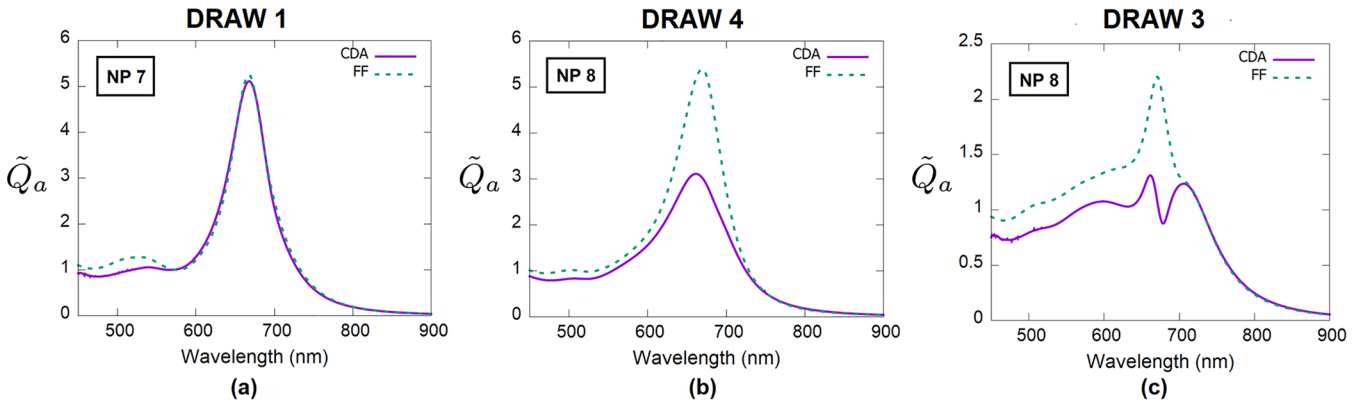

Figure 7. Dimensionless absorption spectra of individual NPs: NP 7 of draw 1 (a), NP 8 of draw 4 (b), and NP 8 of draw 3 (c). The purple solid lines correspond to the spectra calculated with the coupled dipole approximation method (CDA). The green dotted lines correspond to the spectra obtained with the finite element method (FF).

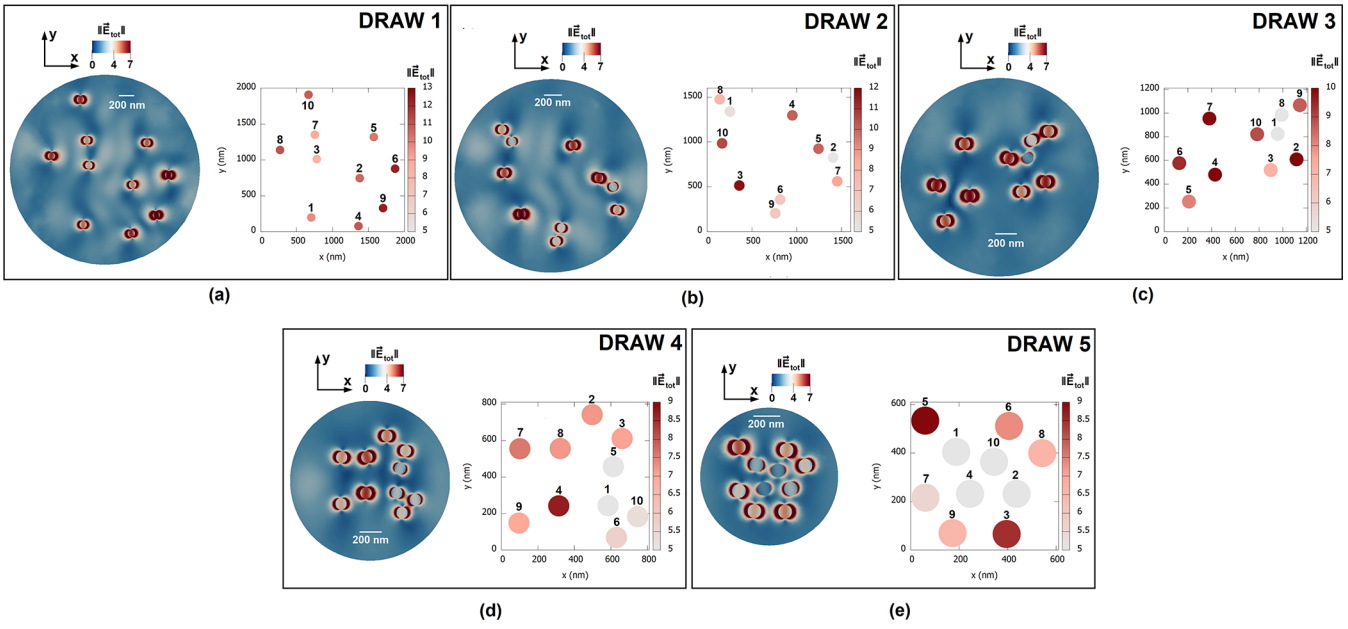

Figure 8. Maps of the total electric field calculated with FreeFEM (left panel, z = 12 nm) and with the CDA (right panel, z = 27.3 nm). The maps are drawn at the wavelength which corresponds to the maximum of the dipolar resonance peaks picked up on the FreeFEM total absorption spectra: (a) draw 1 at λ_{res} = 689 nm, (b) draw 2 at λ_{res} = 683 nm, (c) draw 3 at λ_{res} = 675 nm, (d) draw 4 at λ_{res} = 676 nm, (e) draw 5 at λ_{res} = 677 nm. The color scales have been truncated to allow visualization.

= 1260 nm and d_{ctoc} = 1820 nm. The gold layer participates to the radiative coupling in the far field. Indeed, the inset b of Figure 3 shows that the dielectric layer of the substrate is thin enough for the NPs to "see" the gold layer. The field scattered by the NPs is actually not zero throughout the thickness of the dielectric layer. Moreover, the black dotted line curve in Figure 4 represents the plasmonic response of the dimer deposited on a dielectric substrate (n_2 = 1.5), i.e., in the absence of the gold

https://doi.org/10.1021/acsomega.3c00342
ACS Omega XXXX, XXX, XXX−XXX

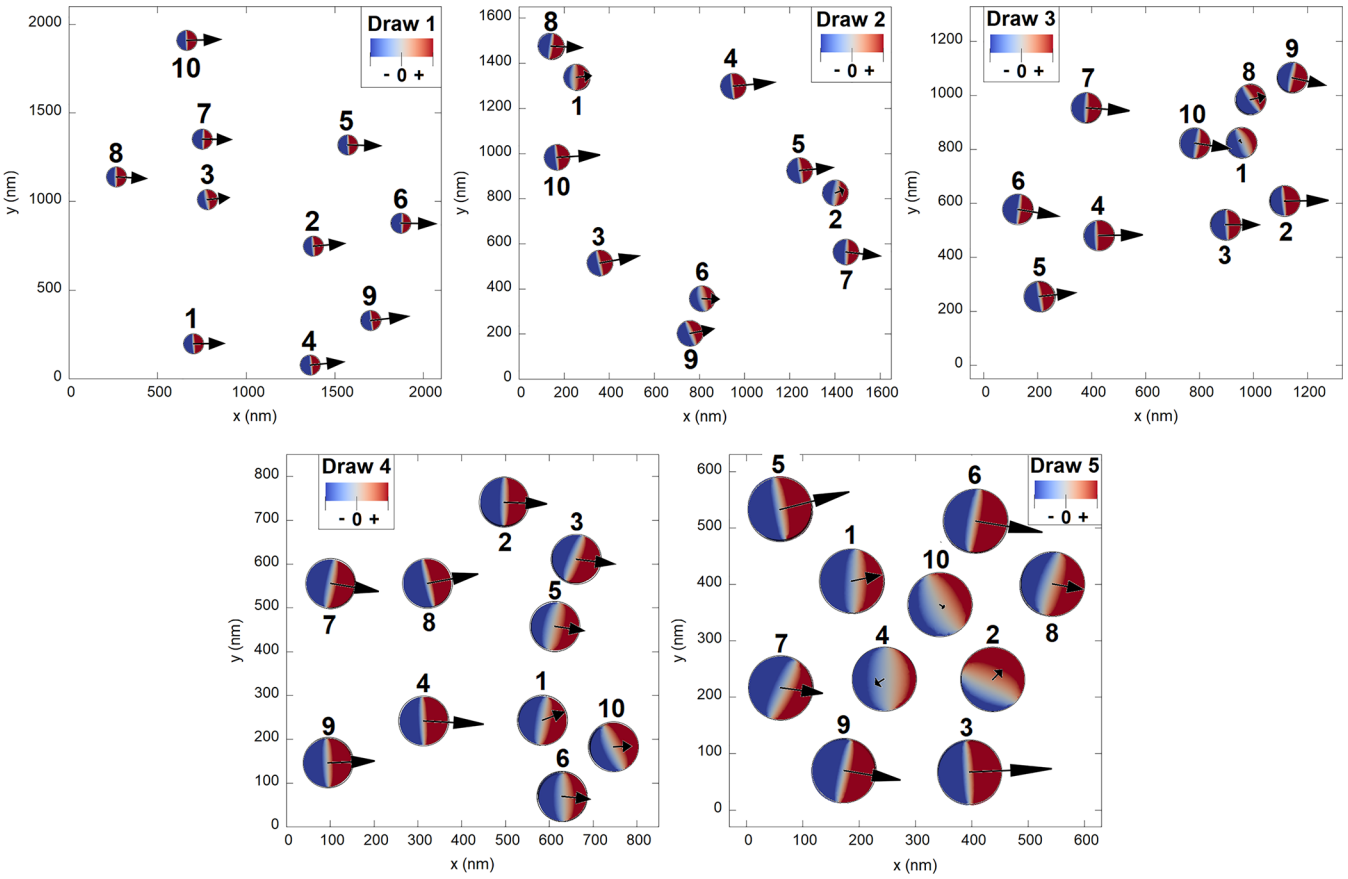

Figure 9. Surface charge distributions calculated with FreeFEM. The color scales have been truncated to allow a better visualization. The black arrows correspond to the real part of the complex dipole moments calculated with the CDA. The maps are drawn at the wavelength which corresponds to the maximum of the dipolar resonance peak identified on the FreeFEM total absorption spectra, i.e., at λ_{res} = 689 nm for draw 1, at λ_{res} = 683 nm for draw 2, at λ_{res} = 675 nm for draw 3, at λ_{res} = 676 nm for draw 4, and at λ_{res} = 677 nm for draw 5.

layer. First, we logically observe lower resonance wavelengths when d_{ctoc} varies due to the decrease of the refractive index. Second, the oscillations generated by the radiative coupling have a significantly smaller amplitude and contrary to what is observed in the presence of gold, they disappear from d_{ctoc} = 1600 nm. The resonance wavelength is then constant and equal to the resonance wavelength of the monomer.

Random Arrangements of 10 Nanoparticles. Figure 6 shows the absorption spectra for 5 different random arrangements of N = 10 NPs. For each draw, the coordinates of the NP centers are randomly selected in a square box of side c_i: c_1 = 2000 nm, c_2 = 1600 nm, c_3 = 1200 nm, c_4 = 800 nm, c_5 = 600 nm. The number of NPs being constant, the arrangements are therefore more and more dense from draw 1 to draw 5 as can be seen in Figure 8. During the draw of the NPs' coordinates, the smallest possible center-to-center distance has been set at d_{ctoc} = 160 nm. We see that the two calculation methods agree on the resonance position of the dipolar mode with an error margin of about ±5 nm. The resonance wavelengths correspond to the values interval found for the dimer at the end of the near-field coupling regime and in the radiative coupling regime. As the arrangements become denser, the absorption decreases, with the exception of draw 3. The shape of the curves obtained using the CDA and FreeFEM agree, although the absorption calculated with the CDA is lower.

If we now consider the absorption spectra, no longer total but individual, we also notice a good agreement between the two methods of calculation. This can be seen for example in Figure 7a for the NP 7 of draw 1 with curves whose dipole resonance peaks overlap almost perfectly. Although being an approximate method, the CDA reproduces the shape of the curves rather well with a few exceptions. We find, as it is the case for the total absorption spectra, NPs for which the absorption evaluated with FreeFEM is greater than the absorption given by the CDA (Figure 7b). The Figure 7c shows another scenario, for the NP 8 of draw 3, where FreeFEM predicts one dipole resonance peak while the CDA gives a double peak whose absorption is much less important. All the individual absorption spectra for the five draws can be viewed in the SI.

The modulus of the total electric field is depicted in Figure 8. The total electric field is the sum of the incident field and the field scattered by the NPs. The maps are drawn at the resonance wavelength, i.e., at the maximum of the dipolar peak, the position of which is identified on the FreeFEM total absorption spectra. For each draw of 10 NPs on Figure 8, the left column shows the map obtained with FreeFEM and the right column shows the map obtained with the CDA. With FreeFEM, the electric field modulus is calculated everywhere in the XY-plane situated at z = 12 nm which approximately corresponds to half the height of the cylinders. With the CDA, it is the electric field inside the NPs which is displayed in the XY-plane at $z = z_{sub}$ = 27.3 nm where the spheroid plane sections are discs. To compare the results given by the two calculation methods, we can first consider the NPs with the least intense electric field. We see a good agreement since the

https://doi.org/10.1021/acsomega.3c00342
ACS Omega XXXX, XXX, XXX−XXX

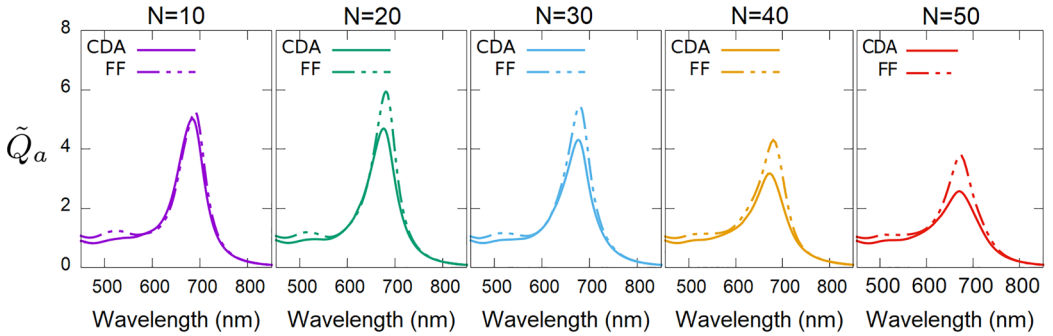

Figure 10. Comparison of the dimensionless absorption efficiency computed with the CDA (solid line) and with FreeFEM (dashed line) for the different arrangements of N = 10, 20, 30, 40, and 50 NPs. For each draw, the coordinates of the NPs' centers are randomly selected in a square box of side c = 2000 nm.

NPs corresponding to this criterion are identical with the two methods. For example, we have the NPs 1 and 2 for draw 2 and the NPs 1 and 8 for draw 3. Both of the calculation methods highlight the appearance of clusters of NPs characterized by a weak electric field when the random arrangements become more compact (draws 4 and 5) or in areas where the NPs are close enough together for the near-field coupling to exist (draw 3). To go further in the analysis, the NPs can be assembled in groups where the modulus of the electric field is roughly the same for all the NPs. We observe a good concordance for all the draws. Indeed, for the draw 1, both the CDA and FreeFEM show that four groups can be defined: (6,9), (10,8,4), (5,2,1), and (7,3) with an increasingly weak electric field. For the draw 2, we have three groups: (10,4,5,3), (8,9,6,7), and (1,2). Moreover, we see with both methods that NP 3 has the most intense field of its group just like NP 7. For the draw 3, there are three groups: (7,10,6,4,2), (9,5,3), and (1,8). There is a slight difference for NP 10, which interacts in the near field with NP 1, as we can see on the FreeFEM map. According to FreeFEM, its electric field is higher than that of NP 7, and according to the CDA, we have the opposite. For the draw 4, FreeFEM gives three groups: (8,4), (9,7,2,3), and (5,1,10,6). Again, there is a difference between the two methods: according to the CDA, the group corresponding to the most intense electric field contains only NP 4. As before, we observe on the map that NP 8 is in near-field coupling with another NP (NP 7). One could therefore ask whether the CDA becomes less precise when the arrangements are dense enough to allow near-field coupling. Nevertheless, the case of NPs 10 and 6 contradicts this hypothesis. Indeed, they are in near-field coupling, and the two methods predict a higher electric field for NP 6. For the draw 5, the NPs at the periphery (5,6,8,3,9,7) have a stronger electric field than the NPs at the center of the arrangement (1,10,2,4). The two methods agree rather well on the intensity of the electric field of the NPs confirming the reliability of the CDA when the pattern becomes denser. The NPs being randomly disposed on the substrate, we see on the Figure 9 that they are not oscillating at the same phase. The colors going from blue to red represent the surface distribution of charges obtained with FreeFEM. The black arrows represent the real part of the induced dipole moment given by the CDA. Although approximate, the coupled dipole method makes it possible to predict the orientation of the dipoles in a rather reliable way. For the draw 1, which is the draw for which the distances between the particles are the greatest, the phase shifts between FreeFEM results and the CDA results are weak for all the NPs. For the draw 2, NP 2 has a larger phase shift and is the one with the smallest dipole moment. In the same way, NP 1 of draw 3 has the largest phase shift and the smallest dipole moment, a trend that we also find for NPs 4 and 10 of draw 5. The discrepancies observed between the FreeFEM and the CDA results shows that it is possible that the CDA has more difficulties in reliably predicting the orientation of weak dipole moments. We can also assume that this limit of the method appears at the level of clusters of NPs organized in a more compact way and characterized by a weak electric field, as can be seen by comparing Figure 8 and Figure 9. Because the NPs with a low dipole moment and a low electric field have a lesser influence on the other NPs, it reduces the impact of the drop in reliability of the CDA which presents remarkable performances given its simplicity.

Random Arrangements of N = 10, 20, 30, 40, and 50 Nanoparticles. This section explores another way to cover the multilayer substrate. The side of the square box, in which the coordinates of the centers of the NPs are randomly selected, is now constant and equal to c = 2000 nm. On the other hand, the number of NPs N is no longer constant but varies from 10 to 50 in steps of 10. Figure 10 shows the total absorption spectra of the systems studied. A good agreement is observed between the two calculation methods with a maximum difference of 7 nm for the position of the dipolar resonance peak. The resonance wavelength decreases slightly when the number of NPs increases. The two methods predict a blue-shift of around 15 nm when going from N = 10 to N = 50. As for the five previous draws including N = 10 NPs, the resonance wavelengths correspond to the value interval found for the dimer at the end of the near-field coupling and in the radiative coupling regime. The resonance wavelength becomes lower than the resonance wavelength of the monomer from N = 20 according to the CDA and from N = 30 nm according to FreeFEM. In addition, there is a decrease in absorption when the number of NPs increases. When we go from N = 10 to N = 50, FreeFEM predicts an absorption decrease around 30% and the CDA predicts a greater decrease of the absorption around 50%. As before, we note that the absorption values at the dipolar resonance provided by FreeFEM are higher than those provided by the CDA.

Regarding the individual absorption spectra, the CDA predicts their shape quite accurately. Concerning the position of the peaks, the difference between the two methods is around ±10 nm in most cases but values around ±20 nm can be found with a frequency of appearance which increases when the arrangements become denser. The NPs present dipolar

https://doi.org/10.1021/acsomega.3c00342
ACS Omega XXXX, XXX, XXX−XXX

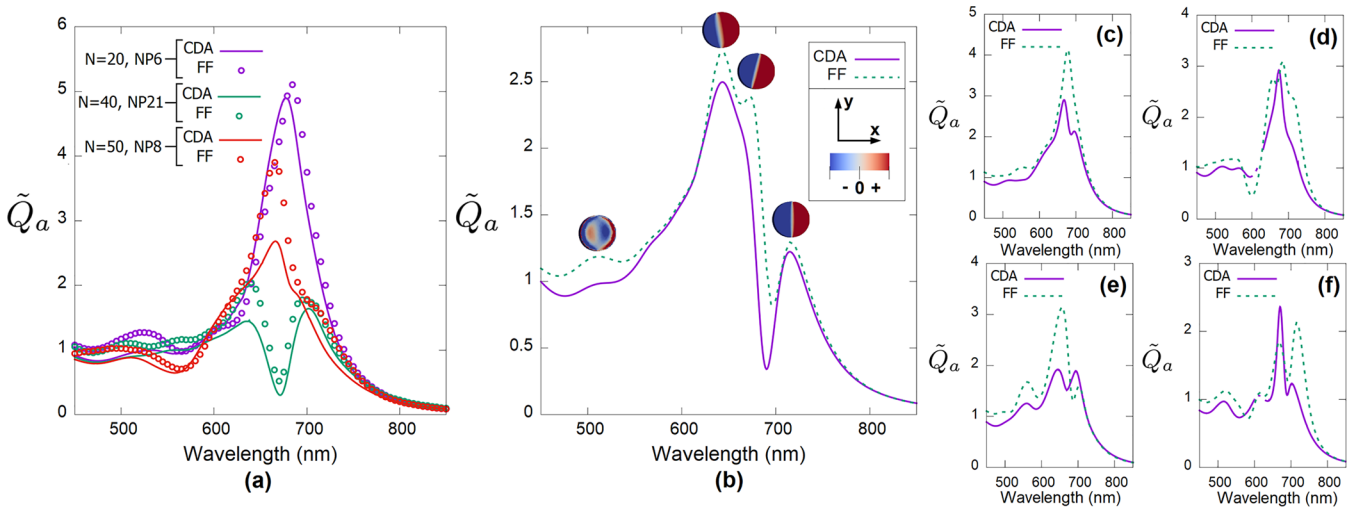

Figure 11. (a) Comparison of the dimensionless absorption efficiency computed with the CDA (solid line) and with FreeFEM (circular dots) for the 6th NP of the arrangement of N = 20 NPs (purple curves), for the 21st NP of the arrangement of N = 40 NPs (green curves), and for the 8th NP of the arrangement of N = 50 NPs (red curves). (b) Absorption spectra of the 29th NP of the arrangement of N = 30 NPs calculated with the CDA (purple continuous line) and with FreeFEM (green dotted line). The surface charge distributions at the upper face of the NP obtained with FreeFEM for the different peaks is also depicted. (c) Absorption spectra of the 25th NP of the arrangement of N = 40 NPs. (d) Absorption spectra of the 15th NP of the arrangement of N = 50 NPs. (e) Absorption spectra of the 30th NP of the arrangement of N = 40 NPs. (f) Absorption spectra of the 30th NP of the arrangement of N = 50 NPs.

resonance peaks shifted toward blue or toward red with respect to the resonance peak obtained for all the NPs of the arrangements. The shifts are about ±10 nm for the wide majority of the NPs and can go up to ±20−25 nm for some NPs. The analysis of the spectra also shows that the CDA method more often tends to underestimate the resonance wavelength compared to FreeFEM. Figure 11(a) gives some examples among all the spectra that are gathered in the SI. For the sixth NP of the draw including N = 20 NPs, FreeFEM and the CDA methods predict a significant dipolar resonance peak respectively at λ_{res} = 684 nm and λ_{res} = 678 nm, values that are very close to the position of the absorption peak of all the NPs ($\lambda_{res,FF}$ = 681 nm, $\lambda_{res,\ CDA}$ = 676 nm). For the 21st NP of the draw including N = 40 NPs, both FreeFEM and the CDA methods provide a split of the dipolar resonance peak with an absorption minimum around 670 nm, whereas on the collective spectra there was an absorption maximum for λ_{res} = 680 nm with FreeFEM and λ_{res} = 673 nm with the CDA. The split of the dipolar resonance peak occurs more frequently as the arrangements become denser which contributes to the height diminution of the collective absorption peak. For the eighth NP of the draw including N = 50 NPs, although there is a significant difference of the absorption maximum at resonance, the two methods give spectra of identical appearance with a dipolar resonance peak presenting 2 shoulders. The increase of the arrangement density is accompanied by an increasingly complex individual plasmonic response with dipole absorption peaks taking on the appearance of two or even three more or less merged peaks (Figure 11 (d)). For this type of plasmonic response, the CDA method does not always give results in agreement with FreeFEM. For example, Figure 11(b) gives the absorption spectra of the 29th NP of the arrangement including N = 30 NPs. We see that the dipolar response is divided into three distinct peaks corresponding to dipolar moments of different directions according to FreeFEM (λ_1 = 644 nm, λ_2 = 673 nm, λ_3 = 717 nm). The CDA for its part predicts only two peaks. Nevertheless there is on the CDA spectrum a shoulder around 673 nm which corresponds to the position of the second dipolar peak on the FreeFEM spectrum. The peak around 510 nm is due the presence of the metallic layer. It seems to correspond to a combination of a dipolar and a breathing mode, which had already been mentioned when studying the plasmonic response of the monomer, also defined as a plasmonic edge mode in the work of Xue et al.[43] The CDA method does not always predict a lower number of peaks than that given by FreeFEM, the reverse can also be observed. This is what we see on the Figure 11(c) where the CDA shows a double peak and FreeFEM a single peak. Nevertheless, for most of the spectra the CDA makes possible to find curves whose appearance is identical to FreeFEM curves although there are significant differences in terms of absorption (Figure 11 (e) and (f)). Figure 12 provides some interesting points about the absorption difference between the two calculation methods at the collective resonance wavelength of the arrangements. The nearest-neighbor separation for each NP of each arrangement is shown on the abscissa axis. This distance corresponds to the minimum of d_{ctoc} for each NP. The absorption difference, depicted on the ordinate axis, is calculated from the following formula:

$$AD_{i,N} = \left.\frac{A_{i,N}^{CDA} - A_{i,N}^{FF}}{A_{i,N}^{FF}}\right|_{\lambda_{res,N}^{FF}} \quad (19)$$

where $AD_{i,N}$ is the absorption difference for the i^{th} NP of the arrangement including N NPs. For each set of NPs, the absorption difference is evaluated at the wavelength $\lambda_{res,N}^{FF}$ which corresponds to the maximum of the dipolar resonance peak picked up on the FreeFEM total absorption spectrum. The absorption values denoted by $A_{i,N}^{CDA}$ and $A_{i,N}^{FF}$ are taken at $\lambda_{res,N}^{FF}$ on the absorption spectrum obtained for each NP i with the CDA and FreeFEM, respectively. We see on the Figure 12 that the nearest-neighbor separation decreases when N increases as the arrangements of NPs become denser. It is

https://doi.org/10.1021/acsomega.3c00342
ACS Omega XXXX, XXX, XXX−XXX

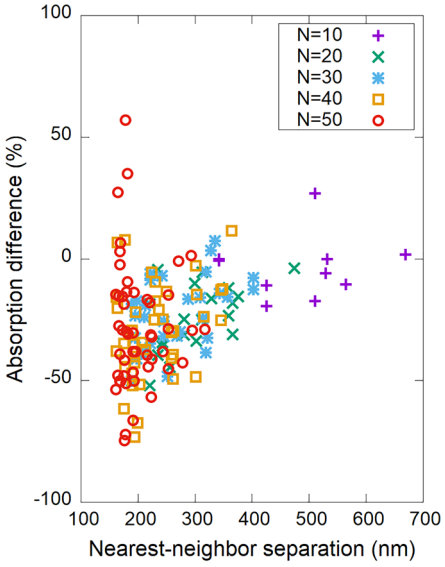

Figure 12. Absorption difference between the CDA and the FreeFEM individual spectra as a function of the nearest-neighbor separation. The points correspond to the values picked up at the wavelengths which correspond to the maximum of the dipolar resonance peak on the FreeFEM total absorption spectra.

also observed that the CDA method tends to provide lower values of the absorption than those of FreeFEM, confirming the previous findings. If we consider the absorption difference less than 35% in absolute value, we notice that 100% of the points are included in this range for N = 10, 80% for N = 20, 87% for N = 30, 63% for N = 40, and 52% for N = 50. Therefore, an increase of the absorption difference is observed when the arrangements become denser with maximum differences that can exceed 70% for N = 40 and N = 50, showing a potential loss of reliability of the CDA method.

As before, we plotted the maps of the total electric field for all the arrangements studied. The maps for the arrangement containing N = 40 NPs are depicted in Figure 13 (a) and (b). The maps for the other arrangements are in the SI. Like for the different draws including N = 10 NPs, there is a good agreement between the two calculation methods. For example, if we consider the group of NPs surrounded by yellow lines, we see that NPs 9 and 26 have a less intense electric field than NPs 8, 31, and 1. For the group of NPs surrounded by orange lines, we observe that NP 39 has an electric field significantly higher than that of NP 2 which is itself characterized by a higher electric field than that of the NP 21. For the five NPs just below, we see that NPs 38, 36, and 5 have a more intense electric field than NPs 34 and 27. For the group of NPs surrounded by pink lines, we observe that NP 20 has an electric field higher than that of the other NPs. Nevertheless, we note that FreeFEM predicts a greater contrast than the CDA. For the three NPs just below, the two methods show that the electric field is the most intense for NP 40 and the least intense for NP 30. For the group of NPs surrounded by green lines, we notice that NPs 19, 12, and 35 have an electric field significantly higher than that of NPs 10, 23, and 7. For the NPs surrounded by white lines, we observe that NPs 11 and 13 have a greater electric field than other NPs. For the remaining NPs, we observe a difference in intensity between the groups of NPs (14,6) and (29,17,15,22,18) on the map obtained with FreeFEM which is not particularly visible on the map obtained with the CDA. However, we find a remarkable concordance between the maps provided by the two methods. Due to the randomness of the arrangements, there are attractive and repulsive interactions between the surface charges of the NPs. This results in a reduction or an enhancement of the dipolar moments, as we can see in Figure 14(a). Furthermore, the dipole moment orientation of the NPs varies with respect to the orientation of the incident electric field, which is polarized along the (Ox) axis. We calculated the deviation of the dipole orientation as follows:

$$D_i = \arctan\left(\frac{\Re(p_{i,y})}{\Re(p_{i,x})}\right), \quad i = 1, N \tag{20}$$

Figure 14(b) indicates that the deviation of the dipole orientation tends to zero degree when the nearest-neighbor separation increases. As the arrangements become denser, the more the orientation of the dipoles varies and the less the

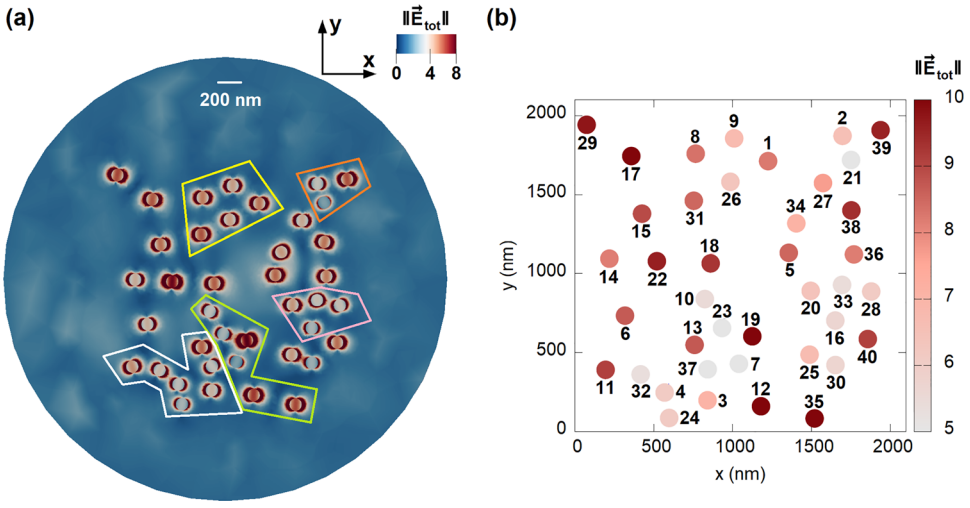

Figure 13. Maps of the total electric field for the arrangement including N = 40 NPs calculated with FreeFEM (z = 12 nm) (a) and calculated with the CDA method (z = 27.3 nm) (b). The maps are drawn at the wavelength which corresponds to the maximum of the dipolar resonance peak on the FreeFEM total absorption spectra, that is λ_{res} = 680 nm. The color scales have been truncated to allow visualization.

https://doi.org/10.1021/acsomega.3c00342
ACS Omega XXXX, XXX, XXX−XXX

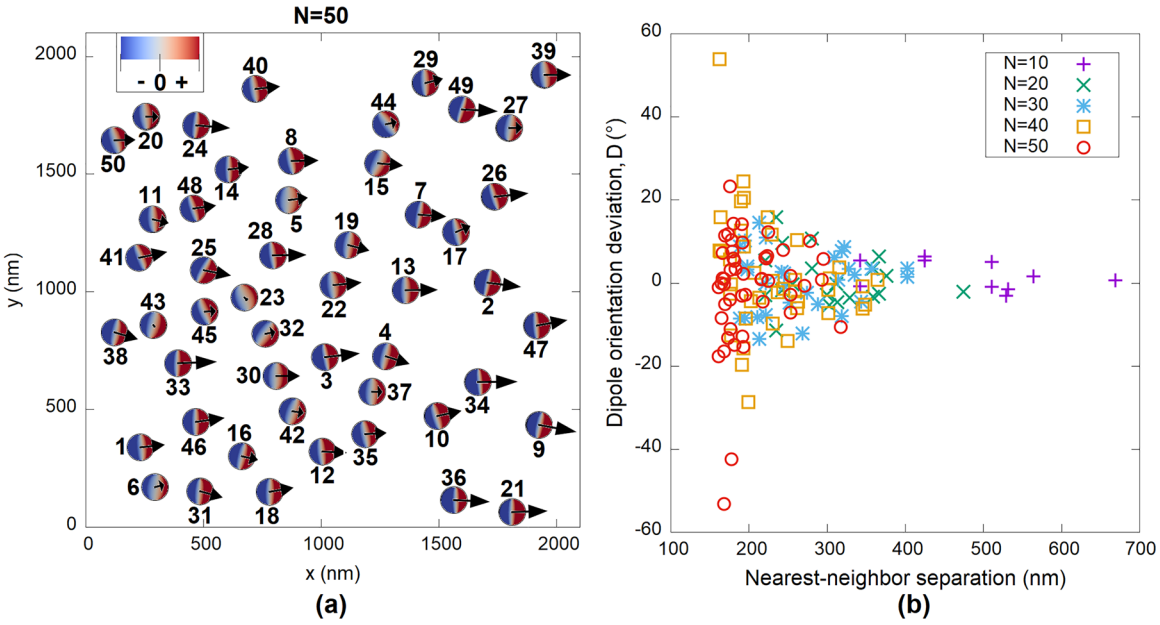

Figure 14. (a) Surface charge distribution of the arrangement including N = 50 NPs calculated with FreeFEM. The color scale has been truncated to allow a better visualization. The black arrows correspond to the real part of the complex dipole moments calculated with the CDA. The map is drawn at the wavelength which corresponds to the maximum of the dipolar resonance peak identified on the FreeFEM total absorption spectrum, i.e., at λ_{res} = 672 nm. (b) Deviation of the dipole orientation with respect to the polarization of the incident electric field as a function of the nearest-neighbor separation.

polarization of the incident electric field has an influence. The comparison of the surface charge distributions calculated by FreeFEM and the dipolar moments given by the CDA shows a good agreement between the two calculation methods. However, the phase shifts between the FreeFEM and the CDA results become more frequent and significant as the arrangement density increases. As before for the draws containing N = 10 NPs, we notice that the significant phase shifts are more often associated with small dipolar moments. Note that only the graph for the arrangement including N = 50 NPs is shown here. The graphs for the other arrangements can be viewed in the SI. It can be seen on those graphs that NPs with a larger dipole moment can also present a significant phase shift like NP 21 of the arrangement containing N = 30 NPs (see Figure S15(b) of the SI).

CONCLUSION

The different simulations realized show that the CDA method is able to predict quite accurately the plasmonic response of metallic nanocylinders randomly deposited on a substrate. The method gives a good evaluation of the absorption spectra shape and of the position of the dipolar resonances. It should be noted that the CDA tends to give values of the absorption and resonance wavelengths lower than those provided by FreeFEM. Increasing the density of the NPs arrangements makes the absorption spectra of the individual NPs more complicated with two or three dipolar resonance peaks more or less merged. The CDA presents a potential loss of reliability in this case which requires vigilance when studying very dense arrangements. Indeed, the CDA has some difficulties when predicting the height of the absorption peaks for denser arrangements. We also observe an increase of the differences between the resonance positions given by the CDA and those given by FreeFEM not exceeding ±20 nm. However, the two calculation methods provide most of the time spectra which are identical in appearance. Another point to be vigilant about is the size of the NPs. Despite the presence of electrodynamic corrections in the polarizability tensor to be able to study NPs whose size does not satisfy the quasi-static approximation, it is possible that these corrections are no longer sufficient if the NPs become too large. It is consequently preferable to check the monomer absorption spectrum with another calculation method before studying the whole system. To obtain a better match, it is possible to adjust the lengths of the semiaxes of the spheroid (a, c) as well as the height of the space between the NP and the substrate (l). Comparing how the two methods follow the evolution of the dipolar resonance wavelength for the dimer in the case of near- and far-field coupling can also be judicious.

These precautions being taken, the CDA constitutes a very interesting method due to its advantages such as its lower memory demand and its reduced computation time. In fact, for the systems studied here our FreeFEM program gives the results in 1 to 3 days while our CDA program gives the results in 20 min to 11 h. It is the evaluation of the indirect Green tensor $\bar{\bar{G}}^{I}$ which increases the computation time. Indeed, the more the system studied contains NPs, the greater the number of Sommerfeld integrals to process. Moreover, since the CDA requires much less memory resources, it is possible to launch many more calculations simultaneously than with FreeFEM. This makes it possible to test and understand more quickly what parameters influence the physical properties of a metasurface. It facilitates the study of random distributions of metallic NPs which are promising inexpensive platforms. Indeed, Anăstăsoaie et al.[44] have recently shown that biosensors based on random plasmonic metasurfaces can have a fluorescence enhancement factor comparable to that which artificially engineered metasurfaces realized by micro- and nanofabrication techniques achieve. Random patterns of plasmonic NPs are also a good approach to produce optical

https://doi.org/10.1021/acsomega.3c00342
ACS Omega XXXX, XXX, XXX−XXX

physically unclonable functions (O-PUFs).[45] PUFs are emerging security objects which can be used as anticounterfeit labels. Their random feature is comparable to fingerprints, and they produce a specific response when challenged. In the case of O-PUFs, the challenge is the incident light. Thus, these few examples show that the CDA could be very useful in identifying high-performance solutions for a desired application in a vast design space.

■ ASSOCIATED CONTENT

Supporting Information

The Supporting Information is available free of charge at https://pubs.acs.org/doi/10.1021/acsomega.3c00342.

Additional details on how to calculate the gold relative dielectric permittivity and how to use the CDA. Additional figures for comparing the CDA results to FEM results (absorption spectra, electric field maps, surface charge distribution maps, dipolar moment maps). Additional data about FEM convergence for the system including 50 NPs (PDF)

■ AUTHOR INFORMATION

Corresponding Author

Ophélie Saison-Francioso − *UMR CNRS 8520 − Cité Scientifique, Institut d'Électronique, de Microélectronique et de Nanotechnologie, 59652 Villeneuve D'Ascq Cedex, France;* Present Address: Département de Physique, Faculté des Sciences et Technologies, Université de Lille, Bât. P5−59655 Villeneuve D'Ascq, *France;* orcid.org/0000-0002-4134-4497; Email: ophelie.saison-francioso@univ-lille.fr

Authors

Gaëtan Lévêque − *UMR CNRS 8520 − Cité Scientifique, Institut d'Électronique, de Microélectronique et de Nanotechnologie, 59652 Villeneuve D'Ascq Cedex, France;* Present Address: Département de Physique, Faculté des Sciences et Technologies, Université de Lille, Bât. P5−59655 Villeneuve D'Ascq, *France;* orcid.org/0000-0001-6526-2907

Abdellatif Akjouj − *UMR CNRS 8520 − Cité Scientifique, Institut d'Électronique, de Microélectronique et de Nanotechnologie, 59652 Villeneuve D'Ascq Cedex, France;* Present Address: Département de Physique, Faculté des Sciences et Technologies, Université de Lille, Bât. P5−59655 Villeneuve D'Ascq, *France*

Yan Pennec − *UMR CNRS 8520 − Cité Scientifique, Institut d'Électronique, de Microélectronique et de Nanotechnologie, 59652 Villeneuve D'Ascq Cedex, France;* Present Address: Département de Physique, Faculté des Sciences et Technologies, Université de Lille, Bât. P5−59655 Villeneuve D'Ascq, *France*

Complete contact information is available at: https://pubs.acs.org/10.1021/acsomega.3c00342

Notes

The authors declare no competing financial interest.

■ ACKNOWLEDGMENTS

The authors thank the French National Research Agency ANR, as part of the project "RANDOM" (reference ANR-19-CE24-0014), for financial support.

■ REFERENCES

(1) Hutter, E.; Fendler, J. H. Exploitation of Localized Surface Plasmon Resonance. *Adv. Mater.* **2004**, *16*, 1685−1706.

(2) Petryayeva, E.; Krull, U. J. Localized surface plasmon resonance: Nanostructures, bioassays and biosensing—A review. *Anal. Chim. Acta* **2011**, *706*, 8−24.

(3) Amirjani, A.; Sadrnezhaad, S. K. Computational electromagnetics in plasmonic nanostructures. *J. Mater. Chem. C* **2021**, *9*, 9791−9819.

(4) Amirjani, A.; Rahbarimehr, E. Recent advances in functionalization of plasmonic nanostructures for optical sensing. *Microchim. Acta* **2021**, *188*, 57.

(5) Huergo, M.-A.; Schuknecht, F.; Zhang, J.; Lohmüller, T. Plasmonic Nanoagents in Biophysics and Biomedicine. *Adv. Optical Mater.* **2022**, *10*, 2200572.

(6) De Sio, L.; Placido, T.; Comparelli, R.; Curri, M. L.; Striccoli, M.; Tabiryan, N.; Bunning, T. J. Next-generation thermo-plasmonic technologies and plasmonic nanoparticles in optoelectronics. *Prog. Quantum Electron.* **2015**, *41*, 23−70.

(7) Gu, M.; Zhang, Q.; Lamon, S. Nanomaterials for optical data storage. *Nat. Rev. Mater.* **2016**, *1*, 1−14.

(8) Loiseau, A.; Asila, V.; Boitel-Aullen, G.; Lam, M.; Salmain, M.; Boujday, S. Silver-Based Plasmonic Nanoparticles for and Their Use in Biosensing. *Biosens.* **2019**, *9*, 78.

(9) Chen, H.; Kou, X.; Yang, Z.; Ni, W.; Wang, J. Shape- and Size-Dependent Refractive Index Sensitivity of Gold Nanoparticles. *Langmuir* **2008**, *24*, 5233−5237.

(10) Zoric, I.; Zäch, M.; Kasemo, B.; Langhammer, C. Gold, Platinum, and Aluminum Nanodisks Plasmons: Material Independence, Subradiance and Damping Mechanisms. *ACS Nano* **2011**, *5*, 2535−2546.

(11) Valamanesh, M.; Borensztein, Y.; Langlois, C.; Lacaze, E. Substrate Effect on the Plasmon Resonance of Supported Flat Silver Nanoparticles. *J. Phys. Chem. C* **2011**, *115*, 2914−2922.

(12) Lamprecht, B.; Schider, G.; Lechner, R. T.; Ditlbacher, H.; Krenn, J.; Leitner, A.; Aussenegg, F. R. Metal Nanoparticle Gratings: Influence of Dipolar Particle Interaction on the Plasmon Resonance. *Phys. Rev. Lett.* **2000**, *84*, 4721−4724.

(13) Liang, Y.; Cui, W.; Li, L.; Yu, Z.; Peng, W.; Xu, T. Large-Scale Plasmonic Nanodisk Structures for a High Sensitivity Biosensing Platform Fabricated by Transfer Nanoprinting. *Adv. Optical Mater.* **2019**, *7*, 1801269.

(14) Wu, Y.; Wang, X.; Wen, X.; Zhu, J.; Bai, X.; Jia, T.; Yang, H.; Zhang, L.; Qi, Y. Surface-enhanced Raman scattering based on hybrid surface plasmon excited by Au nanodisk and Au film coupling structure. *Phys. Lett. A* **2020**, *384*, 126544.

(15) Burford, N. M.; Evans, M. J.; El-Shenawee, M. O. Plasmonic nanodisk thin-film terahertz photoconductive antenna. *IEEE Transactions on Terahertz Science and Technology* **2018**, *8*, 237−247.

(16) Sterl, F.; Herkert, E.; Both, S.; Weiss, T.; Giessen, H. Shaping the color and angular appearance of plasmonic metasurfaces with tailored disorder. *ACS Nano* **2021**, *15*, 10318−10327.

(17) Zhang, F.; Tang, F.; Xu, X.; Adam, P.-M.; Martin, J.; Plain, J. Influence of order-to-disorder transitions on the optical properties of the aluminum plasmonic metasurface. *Nanoscale* **2020**, *12*, 23173−23182.

(18) Vynck, K.; Burresi, M.; Riboli, F.; Wiersma, D. S. Photon management in two-dimensional disordered media. *Nature materials* **2012**, *11*, 1017−1022.

(19) Kang, S. J.; Lee, S. Y.; Lee, K. M. Performance comparison of OpenMP, MPI, and MapReduce in practical problems. *Advances in Multimedia* **2015**, *2015*, 7−7.

(20) Quinto, M.; Boutami, S.; Hazart, J. Fast computation of dipole radiation in stratified background using graphics processing unit. *Progress In Electromagnetics Research M* **2011**, *20*, 115−126.

(21) Ahmed, A.; Pelton, M.; Guest, J. R. Understanding How Acoustic Vibrations Modulate the Optical Response of Plasmonic Metal Nanoparticles. *ACS Nano* **2017**, *11*, 9360−9369.

(22) Koutromanos, I.; McClure, J.; Roy, C. *Fundamentals of Finite Element Analysis: Linear Finite Element Analysis*; John Wiley & Sons: Hoboken, 2018.
(23) Jin, J.-M. *Theory and Computation of Electromagnetic fields*; John Wiley & Sons: Hoboken, 2010.
(24) Hecht, F. New Development in FreeFem++. *J. Numer. Math.* **2012**, *20*, 251−266.
(25) Geuzaine, C.; Remacle, J.-F. Gmsh: A 3-D Finite Element Mesh Generator with Built-In Pre- and Post-Processing Facilities. *Int. J. Numer. Meth. Eng.* **2009**, *79*, 1309−1331.
(26) Saison-Francioso, O.; Lévêque, G.; Akjouj, A. Numerical modeling of acousto-plasmonic coupling in metallic nanoparticles. *J. Phys. Chem. C* **2020**, *124*, 12120−12133.
(27) Kahnert, F. M. Numerical Methods in Electromagnetic Scattering Theory. *J. Quant. Spectrosc. Radiat. Transfer* **2003**, *79*−*80*, 775−824.
(28) Mishchenko, M. I. *Electromagnetic Scattering by Particles and Particle Groups: An Introduction*; Cambridge University Press: Cambridge, 2014.
(29) Nédélec, J. C. Mixed finite elements in R3. *Num. Math.* **1980**, *35*, 315−341.
(30) Chew, W. C. *Waves and fields in inhomogeneous media*; IEEE Press: New York, 1994.
(31) Moroz, A. Depolarization field of spheroidal particles. *J. Opt. Soc. Am. B* **2009**, *26*, 517−527.
(32) Craig F. Bohren, D. R. H. *Absorption and Scattering of Light by Small Particles*; John Wiley & Sons, Inc.: New York, 1983.
(33) Paulus, M.; Martin, O. J. F. Light propagation and scattering in stratified media: a Green's tensor approach. *J. Opt. Soc. Am. A* **2001**, *18*, 854−861.
(34) Paulus, M.; Gay-Balmaz, P.; Martin, O. J. F. Accurate and efficient computation of the Green's tensor for stratified media. *Phys. Rev. E* **2000**, *62*, 5797−5807.
(35) Cho, S. K. *Electromagnetic Scattering*; Springer-Verlag: New York, 1990.
(36) Sipe, J. E. New Green-function formalism for surface optics. *J. Opt. Soc. Am. B* **1987**, *4*, 481−489.
(37) Markel, V. A. Extinction, scattering and absorption of electromagnetic waves in the coupled-dipole approximation. *J. Quant. Spectrosc. Radiat. Transfer* **2019**, *236*, 106611.
(38) Krug, M. K.; Reisecker, M.; Hohenau, A.; Ditlbacher, H.; Trügler, A.; Hohenester, U.; Krenn, J. R. Probing plasmonic breathing modes optically. *Appl. Phys. Lett.* **2014**, *105*, 171103.
(39) Schmidt, F.-P.; Ditlbacher, H.; Hohenester, U.; Hohenau, A.; Hofer, F.; Krenn, J. R. Dark Plasmonic Breathing Modes in Silver Nanodisks. *Nano Lett.* **2012**, *12*, 5780−5783.
(40) Movsesyan, A.; Muravitskaya, A.; Castilla, M.; Kostcheev, S.; Proust, J.; Plain, J.; Baudrion, A.-L.; Vincent, R.; Adam, P.-M. Hybridization and dehybridization of plasmonic modes. *J. Phys. Chem. C* **2021**, *125*, 724−731.
(41) Weber, D.; Albella, P.; Alonso-Gonzalez, P.; Neubrech, F.; Gui, H.; Nagao, T.; Hillenbrand, R.; Aizpurua, J.; Pucci, A. Longitudinal and transverse coupling in infrared gold nanoantenna arrays: long range versus short range interaction regimes. *Opt. Express* **2011**, *19*, 15047−15061.
(42) Rechberger, W.; Hohenau, A.; Leitner, A.; Krenn, J. R.; Lamprecht, B.; Aussenegg, F. R. Optical properties of two interacting gold nanoparticles. *Opt. Commun.* **2003**, *220*, 137−141.
(43) Xue, H.-J.; Jin, F.-C.; Wei, L.-M.; Wang, X.-M.; Hao, D.-P. Plasmonic Edge, Centre and Breathing Modes in Two-Dimensional Disks. *Plasmonics* **2021**, *16*, 471−476.
(44) Anăstăsoaie, V.; Tomescu, R.; Kusko, C.; Mihalache, I.; Dinescu, A.; Parvulescu, C.; Craciun, G.; Caramizoiu, S.; Cristea, D. Influence of Random Plasmonic Metasurfaces on Fluorescence Enhancement. *Materials* **2022**, *15*, 1429.
(45) Smith, A. F.; Patton, P.; Skrabalak, S. E. Plasmonic Nanoparticles as a Physically Unclonable Function for Responsive Anti-Counterfeit Nanofingerprints. *Adv. Funct. Mater.* **2016**, *26*, 1315−1321.

https://doi.org/10.1021/acsomega.3c00342
ACS Omega XXXX, XXX, XXX−XXX